A Numerical Study of a Mesoscale Convective System during TOGA COARE. Part I: Model Description and Verification

Badrinath Nagarajan and M. K. Yau

Department of Atmospheric and Oceanic Sciences, McGill University, Montreal, Quebec, Canada

Da-Lin Zhang

Department of Meteorology, University of Maryland, College Park, Maryland

ABSTRACT

A 16-h numerical simulation of the growing and mature stages of the 15 December 1992 Tropical Ocean Global Atmosphere Coupled Ocean–Atmosphere Response Experiment (TOGA COARE) mesoscale convective system (MCS) is performed to demonstrate the predictability of tropical MCSs when initial conditions and model physical processes are improved. The MCS began with two entities S_1 and S_2, which developed and eventually merged to form a large anvil cloud.

To obtain a realistic simulation of the MCS, the initial moisture field in the operational European Centre for Medium-Range Weather Forecasts (ECMWF) analysis is improved, based on previous findings. The deep column ascent and surface potential temperature dropoff (SPTD) are implemented into the initiation mechanism of the Kain–Fritsch cumulus parameterization scheme (KF CPS). Other refinements to the KF CPS include the introduction of the accretion process in the formation of convective rain and the detrainment of rain and ice particles at the cloud top.

With the improved initial conditions and model physics, the modeled MCS shows many features similar to the observations, including the evolution of the anvil cloud fraction, the three convective onsets at three different times during the growing stage, and the characteristics of two deep convective lines during the mature stage. A series of sensitivity tests indicates that the SPTD is largely responsible for the successful prediction of the life cycle of the MCS, while inclusion of the deep column ascent criterion yields a better timing for the onset of the mature stage.

The effects of modifying the initial moisture field are also investigated.

1. Introduction

The warm pool, characterized by sea surface temperatures (SSTs) in excess of 29°C, experiences considerable diabatic heating throughout much of the overlying atmosphere and receives the largest mean annual rainfall in the world [3–5 m yr^{-1}; see Webster and Lukas (1992)]. The diabatic heating, accompanied by the freshwater flux into the ocean, is realized through deep convective processes modulated on timescales ranging from diurnal up to 30–40 days. In particular, supercloud clusters (Nakazawa 1988) or multiday clusters (Mapes and Houze 1993b), associated with the Madden–Julian oscillation (MJO), represent the largest spatial and temporal scales. Tropical cloud clusters or mesoscale convective systems (MCSs) exhibit intermediate scales,

whereas individual convective cells occur at the smallest scale.

Sui et al. (1997) suggested that to successfully simulate the multiscale variations in the MJO, both the atmospheric convective processes on the diurnal timescale and ocean mixed layer processes must be resolved. To understand the atmospheric convective processes, it is necessary to clarify how convection is organized. Webster and Lukas (1992) consider this as a "zeroth order" problem. Specifically, the life cycle of MCSs, including the initiation, growing, mature, and dissipating stages must be understood. Note that Tollerud and Esbensen (1985) distinguished the life cycle of an MCS from that of a mesoscale precipitation feature (MPF). They defined an MCS as being composed of one or more MPFs that appear as entities in radar reflectivity. Thus MPFs represent the mesoscale organization of an MCS (Leary and Houze 1979).

A number of studies have been carried out to examine the life cycles of MCSs that occurred during the Global Atmospheric Research Programme (GARP) Atlantic

---

Corresponding author address: Dr. Badrinath Nagarajan, Department of Atmospheric and Oceanic Sciences, McGill University, 805 Sherbrooke W., Montreal, PQ H3A 2K6, Canada.
E-mail: badri@zephyr.meteo.mcgill.ca

Tropical Experiment (GATE; Houze and Betts 1981). The growing, mature, and dissipating stages were identified on the basis of area-averaged (about 1000 km²) vertical velocity (Nitta 1977), and anvil cloud fraction data (Tollerud and Esbensen 1985). The growing stage is dominated by convective cells and characterized by maximum vertical motion in the lower troposphere. During the mature stage, the strongest vertical motion shifts to the upper troposphere, because of the development of upward motion in the anvil region. During the dissipation stage, the upward motion collapses in the lower troposphere but remains in the upper troposphere.

Leary and Houze (1979) documented the life cycles of MPFs during GATE, and Sherwood and Wahrlich (1999) studied it over the warm pool using satellite data. In the initiation stage, also referred to as the convective onset, an MPF takes the form of a line of cumulonimbus cells oriented perpendicular to the low-level flow. Raymond (1995) suggested that the warm-pool deep convection is initiated when the convective deficit, defined as the difference between the saturation equivalent potential temperature of the cloud layer and the boundary layer equivalent potential temperature (i.e., $\theta_{et} - \theta_{eb}$), is close to zero. He proposed that the warm pool convection is regulated by a balance between the tendencies of surface fluxes and convective downdrafts, which act to increase and decrease θ_{eb}, respectively.

During the growing stage, new convective cells develop between and ahead of existing cells in the outflow regions of convective downdrafts. In the upper troposphere, an overhang of cloud and precipitation particles from convective updrafts extends downwind in the outflow layer. During the mature stage, an MPF is characterized by a region of convective cells along its leading edge and a large area of stratiform precipitation to the rear. The stratiform rainfall is maintained by organized mesoscale updrafts in the trailing anvil clouds. Beneath the anvil clouds, cooling due to evaporation (melting) of falling rain (ice) drives mesoscale downdrafts. In the dissipating stage, convective cells cease to form along the leading edge but the stratiform precipitation persists for at least several hours longer.

During the life cycles of MPFs, complex interaction, such as mergers and splits among MPFs, were noted. This interaction was referred to as the gregarious behavior of tropical convection (Mapes 1993) and may be associated with gravity waves from deep convection. Mapes (1993) showed that by specifying a heating profile similar to that observed in a tropical MCS, the compensating subsidence required to balance the upward mass flux sets off gravity waves that produce upward displacements in the lowest 4 km in the mesoscale vicinity of the heated region. Air parcels in the atmospheric boundary layer (ABL) are lifted to reach their level of free convection, thereby promoting new convection in the mesoscale vicinity.

Although numerous observational studies of MCSs or MPFs over the Tropics have been conducted (e.g.,

Mapes and Houze 1993a; Kingsmill and Houze 1999; Sherwood and Wahrlich 1999), few numerical simulations initialized with three-dimensional observations have been performed to study their life cycle, particularly over the warm pool. The successful prediction of tropical MCSs or MPFs at the right location and time still remains a challenge to atmospheric scientists due partly to the paucity of observations with adequate spatial coverage and partly to the lack of understanding of the warm pool convective onset processes. The problem of convective onsets is compounded by the failure of traditional convective indices and the occurrence of sufficient convective available potential energy (CAPE) 90% of the time (Sherwood 1999). This also hinders real-data simulation studies whose success critically depends on correctly predicting the convective onsets (Kain and Fritsch 1992; Zhang and Fritsch 1986b; Stensrud and Fritsch 1994).

The objectives of this paper are to (i) document the modifications and improvements of the model physics and initial conditions for simulating tropical MCSs over the warm pool, (ii) successfully simulate the life cycle of a tropical MCS with the improved model physics and initial condition, and (iii) provide verification of the model simulation in order to establish credibility for some diagnostic results to be presented in subsequent parts of this series of papers. The next section provides an overview of the MCS that occurred on 15 December 1992 during the Tropical Ocean Global Atmosphere Coupled Ocean–Atmosphere Response Experiment (TOGA COARE). Section 3 describes the improvements to the model physics and the initial moisture field. Section 4 presents the verification of the control (CTL) simulation against available observations obtained from wind profilers, Geostationary Meteorological Satellite (GMS), and airborne Doppler radar. Section 5 contains the sensitivity of the simulation results to the convective initiation mechanisms and the modifications to the initial moisture field. A summary and conclusions are given in the final section.

2. Case overview

The MCS under investigation was initiated at 0530 UTC 15 December 1992 and lasted till 2330 UTC the same day. Its evolution can be traced using the Japanese GMS infrared (IR) imagery, as given in Figs. 1a–d. Early in the life cycle, the MCSs were composed of entities S_1 and S_2 (Fig. 1a), which developed individually and attained an approximate size of 250 km by 1023 UTC (Fig. 1b). At 1231 UTC (Fig. 1c) S_1 and S_2 began to merge into an MCS as new convection developed between the two entities. The MCS exhibited a large cloud shield at 1831 UTC (Fig. 1d).

The large-scale synoptic setting was typical of the Australian monsoon season. McBride et al. (1995) and Lin and Johnson (1996) documented westerly wind burst (WWB) events during the TOGA COARE inten-
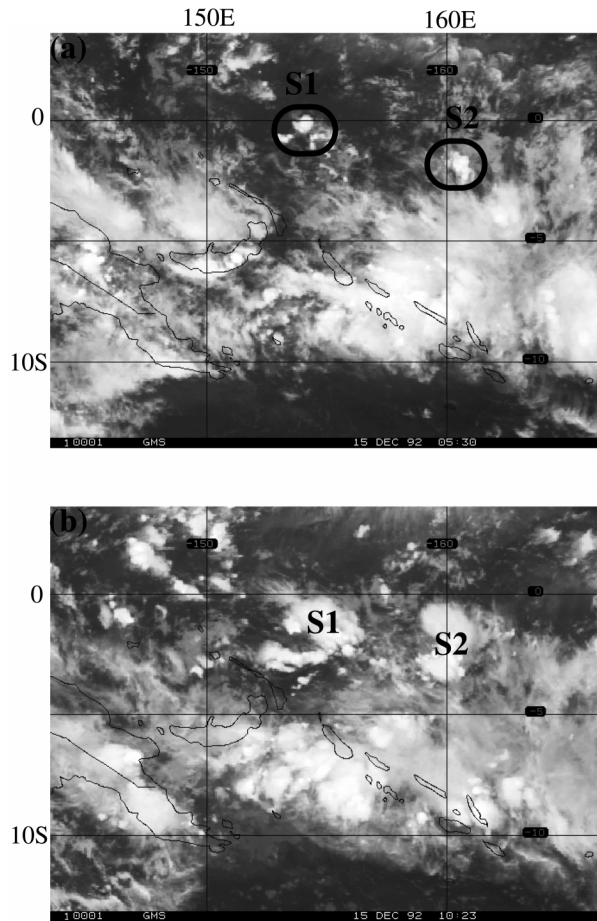
FIG. 1. Japanese GMS infrared image over the study area depicting the development of two systems denoted by S1 and S2 at (a) 0530 and (b) 1023 UTC 15 Dec 1992, respectively. Their merging and the mature stage of the merged MCS occur at (c) 1231 and (d) 1831 UTC, respectively.

FIG. 1. (*Continued*)

sive observation period (IOP), with one WWB event peaking on 1 January 1993. Thus, the MCS occurred 2 weeks prior to the peak westerly wind burst. In a study of the characteristics of 4–20-day oscillations during the TOGA COARE IOP, Numaguti (1995) reported the absence of significant wave activity at 850 and 200 hPa in the region 0–5°S and 155–160°E. Since the wave activity was confined to 190°–240°E after 23 November 1992, the effects of the 4–20-day tropical wave on the evolution of the MCS are expected to be small.

The European Centre for Medium-Range Weather Forecasts (ECMWF) analyses at 0000 UTC 15 December 1992 (i.e., 4–5 h before the onset of S_1 and S_2) indicate moderate values of CAPE and favorable upward motion near 5°S, 160°E and 3°S, 145°E (Fig. 2a), where two MCSs were present at 0530 UTC (Fig. 1a). However, over the regions where S_1 and S_2 would appear, small CAPE with weak or little vertical motion exists. Nevertheless, the ω field in the vicinity of S_1 and
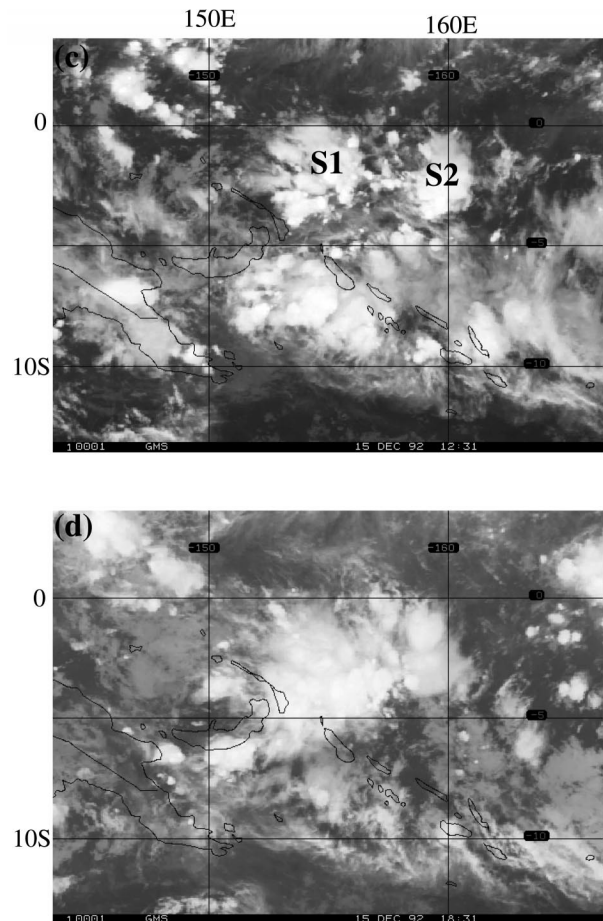
S_2 becomes more favorable with time as is evident in Figs. 2b,c.

Figure 3 shows the time variation of the domain-averaged brightness temperature obtained from the hourly GMS IR imagery. At 0530 UTC, the average brightness temperature was high (i.e., 270 K) due to the presence of mostly low-level clouds at this time (see Fig. 1a). In the interval of 0530–1730 UTC, S_1 and S_2 were initiated, underwent individual development and merged to form a spatially extensive anvil cloud, thus causing a rapid drop in the brightness temperature. This period will be defined as the *growing* stage of the MCS. Between 1700 and 2000 UTC area-averaged brightness temperature further decreased and maintained at about 230–232 K, which is defined as the *mature* stage. After 2000 UTC, there is a rapid increase in brightness temperature, signaling the weakening of convective activity or entering the *dissipation* stage of the MCS. Our classification of various stages of the life cycle is consistent with the results of Miller and Fritsch (1991). In the present study, we focus on only the growing and the mature stages.

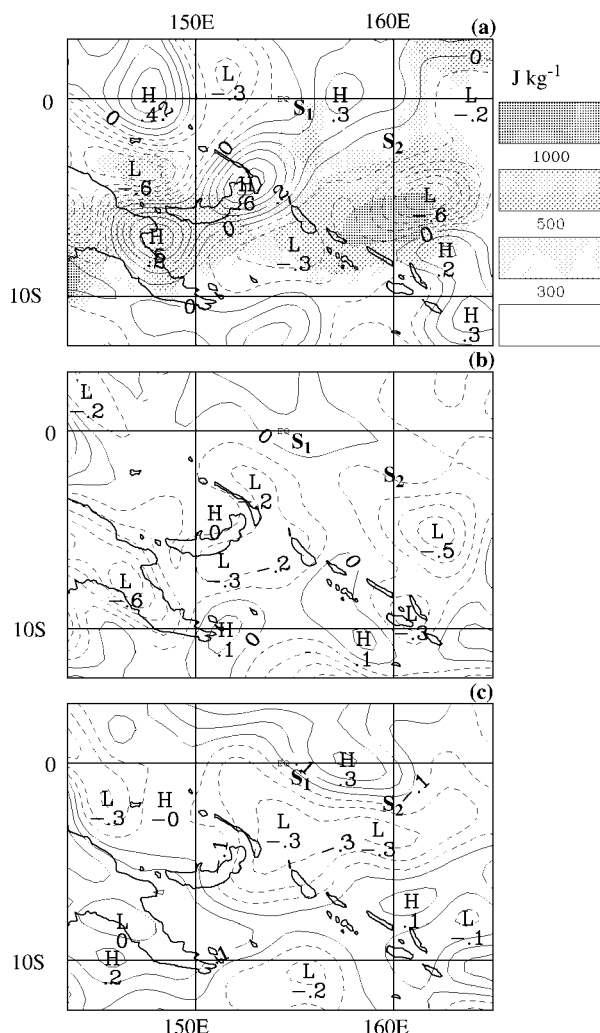Protat et al. (1995, 1998) documented airborne Dopp-

FIG. 2. Horizontal distribution of the 500-hPa vertical velocity (ω) at intervals of 0.1 Pa s^{-1} at (a) 0000, (b) 0600, and (c) 1200 UTC 15 Dec 1992. CAPE in J kg^{-1} (shaded) is superposed in (a). Both ω and CAPE were computed from ECMWF analyses. Solid (dashed) lines represent subsidence (ascending motions). The location of the entities S_1 and S_2 at 0530 UTC are indicated.

FIG. 3. Temporal variation of the area-averaged brightness temperature from the GMS IR imagery. Averaging area is domain C in Fig. 5.

3. Model description and initialization

An improved version of the Mesoscale Compressible Community (MC2) model described by Benoit et al. (1997) is employed. Two domains are used to study the 15 December 1992 MCS through the simulation of its meso-β-scale features (Fig. 5). The coarse-mesh simulation derives its initial and lateral boundary conditions from the ECMWF (1.125° resolution) operational analyses, which is enhanced with radiosonde observations using the Pennsylvania State University–National Center for Atmospheric Research (PSU–NCAR) fifth-generation Mesoscale Model (MM5) preprocessor systems (domain A). The initial and boundary conditions for the fine-mesh simulation are obtained by interpolation from the coarse-mesh simulation (domain B). Except for the model parameters listed in Table 1, all other physical parameters are identical in both simulations. The solar and IR radiation schemes are invoked every 30 min. The ABL processes, including the vertical diffusion, and the explicit microphysics processes (Kong and Yau 1997) are also included. Twenty-five vertical levels were used: 21 20.6, 19 316.8, 17 021.0, 15 859.40, 15 231.00, 14 455.7, 12 839.7, 10 691.0, 8801.37, 7290.4, 5999.7, 4868.9, 3889.69, 3004.3, 2183.0, 1530.0, 1051.0, 683.75, 416.8, 242.76, 139.8, 73.9, 31.6, 13.42, and 0.0 in the Gal-Chen meters (Benoit et al. 1997). The model top is at 25 000 m. The National Centers for Environmental Prediction SST analysis was modified by accounting for convective cooling in regions occupied by MCSs between 0000 UTC and 6 h before. A reduction of 1.75°C in SST is made in MCS regions, in accordance with the observations reported by Hagan et al. (1997).

a. Improvements to physical processes

To obtain a reasonable simulation of the MCS, we found it is necessary to improve some physical repre-

ler radar observations of the MCS during the mature stage. Figure 4 depicts the time composite (1700–2045 UTC) airborne Doppler radar reflectivity data and the retrieved wind field at an altitude of 0.5 km. There were two deep convective lines, designated as L_1 and L_2, with a reflectivity minimum located between them (see Fig. 5 for their distribution with respect to S_1 and S_2). Corresponding to each system is a stratiform precipitation region to the northwest (although less developed for L_2). Protat et al. (1997) computed the vertical motion in the stratiform regions and showed subsidence below the freezing level and upward motions above. A vertical cross section through L_1 and L_2 (not shown) indicates stronger vertical motion for L_1 than L_2 because of the latter being in its decaying stage during this time interval (Protat et al. 1995).
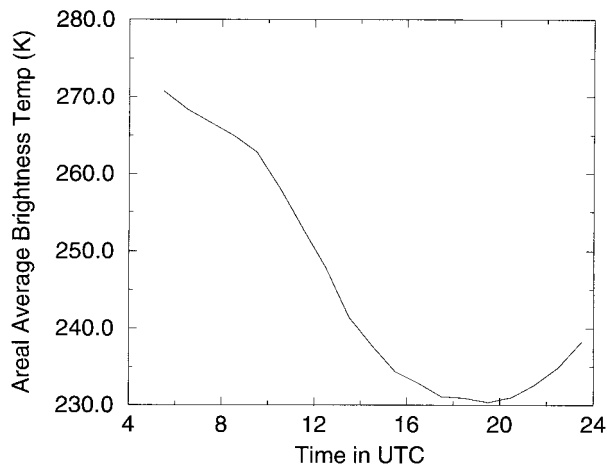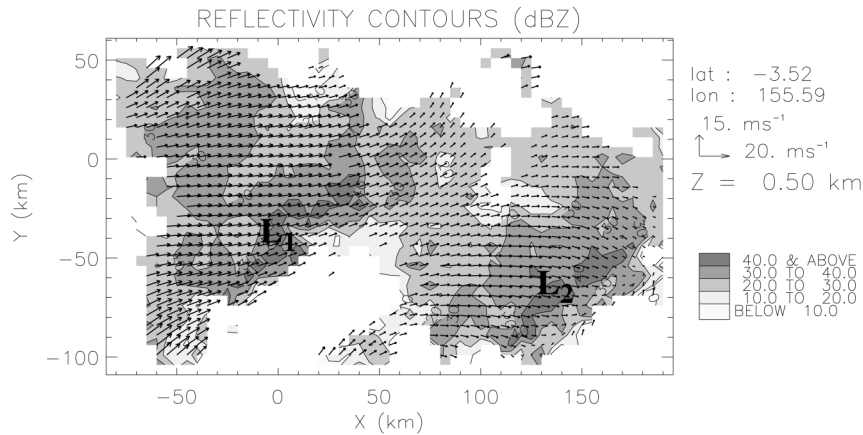
REFLECTIVITY CONTOURS (dBZ)

FIG. 4. Time composite airborne Doppler radar reflectivity (shaded) along with the retrieved wind field at 0.5-km height. The Cartesian grid x axis is rotated 15° clockwise from true east; see domain M in Fig. 5. (Figure courtesy of A. Protat.)

sentation related to cumulus convection and surface fluxes. These include convective initiation, detrainment of cloud water, ice and rainwater in the Kain–Fritsch (KF) cumulus parameterization scheme (CPS), and the modifications suggested by Fairall et al. (1996b) to compute surface fluxes for weak surface flows found over the warm pool. The convective gust effects on the surface fluxes are incorporated following Jabouille et al. (1996).

1) CONVECTIVE INITIATION IN KF CPS

In this study, the Kain–Fritsch trigger (KFT) incorporating the modifications introduced by Zhang and Fritsch (1986b) is employed. The KFT function is described in Fritsch and Chappell (1980). Additional criteria are introduced to account for the small tropical convective inhibition (CIN) values (≤ 10 J kg^{-1}) compared to those reported for midlatitude convection [CIN of 60–100 J kg^{-1}; LeMone et al. (1998)]. First, the latent heating and the upward motion in tropical MCSs tend to induce vertical motion in their ambient ABL due to the propagation of gravity waves (Mapes 1993). This associated lifting can enable an air parcel from the ABL to easily reach its level of free convection, thereby initiating convection. Once deep convection is initiated at a particular location, the adjoining regions are in turn rendered favorable through the lifting mechanism. This may lead to the growth of spurious convection in the model. To mitigate this type of convective initiation, we impose the deep column ascent (DCA) as a necessary condition in which grid-scale upward motion extends at least above 600 hPa.

Second, Raymond (1995) related the occurrence of deep convection over the warm pool with low values of convective deficit. Crook (1996) found convective initiation to be sensitive to surface potential temperature dropoff (SPTD) and surface moisture dropoff. In warmer and moist

environments (such as the warm pool), he suggested that convective initiation is more sensitive to SPTD. Given the importance of SPTD in initiating deep convection over the warm pool, we were led to designing an additional function to be used in conjunction with the KFT function. The SPTD function is defined here as

$$\Delta \theta_{surf} = \theta_{SST} - \overline{\theta}_{ABL}, \qquad (1)$$

where θ_{SST} is the sea surface potential temperature and $\overline{\theta}_{ABL}$ is the ABL mean potential temperature. Crook (1996) defined $\Delta \theta_{surf}$ as the difference between surface air potential temperature and the ABL mean potential temperature. In the model, no superadiabatic layers occur except for the lowest model layer due to the vertical diffusion scheme. We employ θ_{SST} in its place.

Convective inhibition is reduced due to the increase in surface temperature or $\Delta \theta_{surf}$ (Crook 1996). Large $\Delta \theta_{surf}$ increases the probability of convective initiation. Since our objective is restricted to the onset of new convection at a model grid point, we expect the existence of some threshold value of $\Delta \theta_{surf}$ to correlate with the new convective areas. To quantify such a correlation, we define a parameter T as follows. Let G denote the set of grid points where the KFT function is satisfied and the SPTD exceeds a threshold value. Let G1 represent the subset of grid points in G where convective onset also occurs. Defining F as the total number of grid points in G and C the total number of grid points in G1, the parameter T is simply given by the ratio C/F. Note that F decreases as the threshold value for SPTD increases so that initially T also increases. However, for high SPTD threshold values, C may decrease rapidly because the members in G become so few that the chance of intercepting a convective onset area becomes small. As a result, T can decrease for high values of the SPTD threshold.

It is clear that the parameter T, varying between 0 and 1, represents the fraction of the area enclosed by
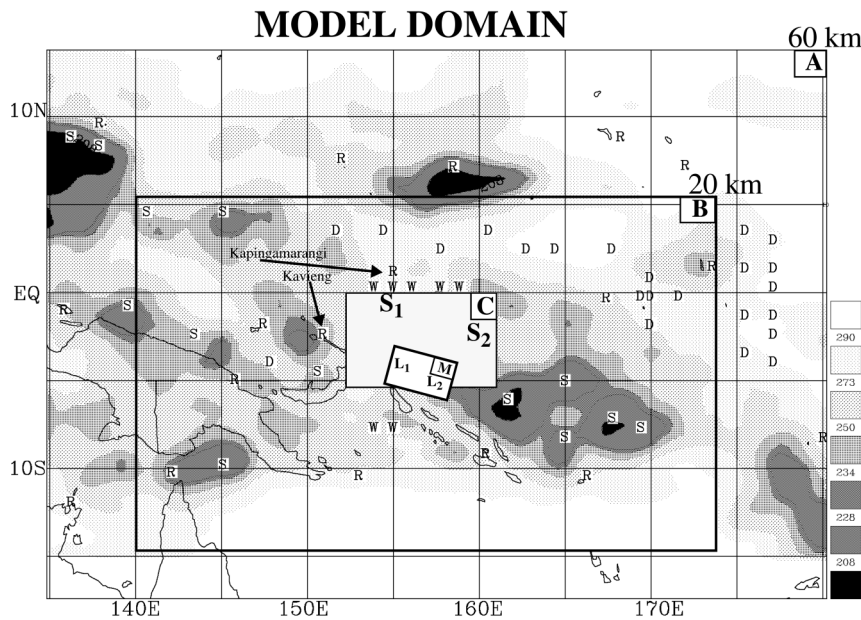
MODEL DOMAIN

FIG. 5. The coarse (A) and fine (B) mesh domains used in model simulation from 0000 to 2000 and 0400 to 2000 UTC, respectively. The shaded domain (C) depicts the approximate region over which the MCS develops and is used to compute domain-average quantities. The Cartesian grid used by Protat et al. (1998) to perform analysis of the airborne Doppler radar data is indicated by domain M. The ISS wind profilers are located at Kapingamarangi and Kavieng. The location of entities S_1 and S_2 at 0530 UTC 15 Dec 1992 and the convective lines L_1 and L_2 observed during the mature stage of the MCS (1700–2045 UTC) are indicated. The 2330 UTC 14 Dec 1992 brightness temperature (K) is shown as shaded areas. The initial moisture field is improved by accounting for the diurnal warming of SST (located at W), the excessive moisture at low levels (located at D), and the midlevel dryness (located at S) in the ECMWF analysis of moisture. The symbol R denotes the radiosonde upper-air data used to enhance the ECMWF analysis at model initial time (0000 UTC 15 Dec 1992).

the SPTD threshold value contour where convective onsets are observed. Sherwood and Wahrlich (1999) used time series of cloud fraction to determine convective onsets from the GMS IR satellite data. The cloud fraction (C_{208}) was defined as the percentage cloudy area with brightness temperature $T_b < 208$ K over a square box 120 km on a side. A convective onset occurs when $C_{208} > 0.05$ at time t but not at any other time within the previous 3 h in the satellite data.

Figure 6 shows the variation of the T parameter with $\Delta\theta_{surf}$ at 0400 UTC 15 December 1992 (i.e., the initial time for the fine mesh). Clearly, T reaches a maximum when SPTD is close to 1.25°C. This value of SPTD is therefore chosen as a necessary condition for deep convection to occur.

Third, various parameters in the KFT function are modified:

1) $W_{klcl} = 0.38$ cm s^{-1} for air parcels originating in the ABL and $W_{klcl} = 0.76$ cm s^{-1} above the ABL. This parameter was originally designed by Zhang and Fritsch (1986b) as a diurnal filter function to eliminate convection triggered due to daytime surface heating.
2) $C_1 = 5.84$°C cm$^{-1/3}$ s$^{1/3}$, which implies that a grid-scale vertical motion of 0.5 cm s^{-1} produces a temperature perturbation of 1°C. This new value for C_1 is based on the consideration of weak vertical motion over the warm pool relative to midlatitudes [for details on this parameter refer to Fritsch and Chappell (1980)].

TABLE 1. The simulation period, grid sizes, time step, and cumulus parameterization scheme (CPS) used for the coarse- and fine-mesh simulations.

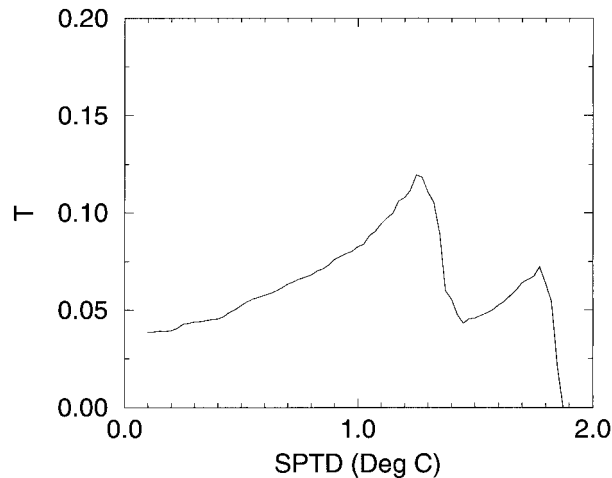| Grid size (Δx, km)	Dimensions (x, y, z)	Simulation period (UTC)	Time step (s)	CPS
60	$85 \times 65 \times 25$	0000–2000	720	Betts and Miller (1993) CPS for deep and shallow convection
20	$189 \times 113 \times 25$	0400–2000	90	Kain and Fritsch (1990) CPS for deep convection, and Betts and Miller CPS for shallow convection

FIG. 6. Variation of the parameter T (the fraction of the area enclosed by the SPTD contour where convective onsets are observed) with the SPTD for 0400 UTC 15 Dec 1992.
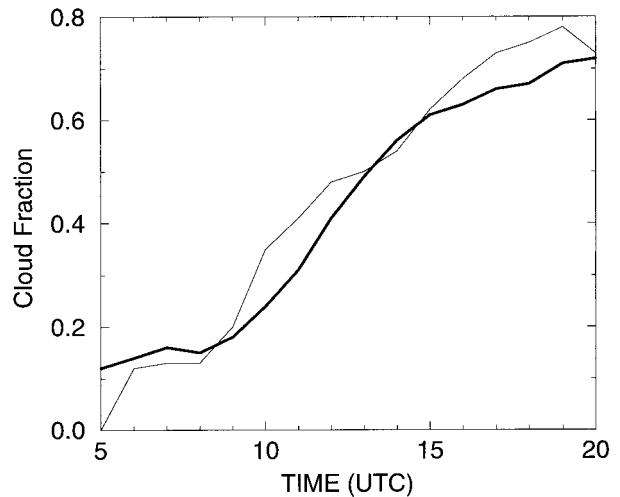

FIG. 7. Evolution of the fractional anvil cloud cover over domain C (see Fig. 5) from hourly GMS infrared imagery (thick solid) and from hourly model simulation (thin solid).

3) Minimum cloud depth is 8 km. This choice is motivated by the results of Rickenbach and Rutledge (1998) who found that convective cloud height distribution is bimodal over the warm pool: one at 8–9 km and the other at 14–15 km. The new value is twice the value originally used (4 km) in the KF CPS.

2) DETRAINMENT OF CLOUD WATER AND ICE (q_c^{KF} AND q_i^{KF})

A significant amount of moisture supply for stratiform precipitation in MCSs originates from deep convective clouds (Leary and Houze 1980). Molinari and Dudek (1992) pointed out that the successful simulation of MCSs depends critically on mid- and upper-tropospheric moisture supply from convective clouds. In the original KF CPS this moisture supply comes from detrainment of hydrometeors that occurs from the cloud base to the cloud top with a magnitude depending on the updraft detrainment rate and layer mean hydrometeor content. In the present study, we assume that detrainment takes place only in a 150–200-hPa layer located below the cloud top. The amount of detrained cloud and ice contents is the accumulated detrainment values for q_c^{KF} and q_i^{KF} between cloud base and cloud top in the original KF CPS. We found that this modification results in a realistic cloud coverage over the model domain compared to GMS IR imagery (see Fig. 7). In addition, we assume that q_c^{KF} exists only when $T > 0°C$ and q_i^{KF} exists when $T < 0°C$.

3) DETRAINMENT OF CONVECTIVE RAIN

Similar to the detrainment of cloud water and ice, the detrainment of convective rain in the original KF CPS is represented by

$$\frac{\Delta q_r^{KF}}{\Delta t} = -\frac{\delta_u q_{ru}}{\Delta p}, \qquad (2)$$

where δ_u is the updraft detrainment rate, Δp is the pressure interval between model levels, and q_{ru} is the mean rainwater mixing ratio in the updraft.

We modified Eq. (2) by adding a term due to the accretion of cloud droplets by raindrops. In the Tropics, warm rain processes occur in deep convective clouds. Autoconversion of cloud water to rain and accretion of cloud water by rain are the two dominant precipitation formation mechanisms. In the KF CPS scheme all convective rain forms from autoconversion. To include the process of accretion, we added a detrainment term for accreted convective rain into Eq. (2) (Kong and Yau 1997):

$$\frac{\Delta q_r^{KF}}{\Delta t} = -\frac{\delta_u q_{ru}}{\Delta p} - \frac{\omega_u q_{ru}|_{acc}}{\Delta p}, \qquad (3)$$

where $\omega_u = -M_u g/\Delta x^2$ is the updraft vertical velocity (in pressure coordinates), M_u is the updraft mass flux, and $q_{ru}|_{acc}$ is the rain mixing ratio associated with accretion.

The mass flux scheme in the KF CPS extracts moisture from a thin layer (about 150 hPa thick) above the cloud base to satisfy the closure regarding the removal of available buoyant energy in the updraft layers. This closure assumption imposes an upper limit on the convective precipitation produced by the KF CPS. Kain and Baldwin (1999), in an attempt to improve the quantitative precipitation forecasts by the KF CPS during heavy rain episodes, suggested that the convective rainfall should be supplemented by grid-resolved precipitation processes. This implies the coexistence of explicit and CPS rain processes (Zhang et al. 1988; Molinari and Dudek 1992). In the present study, we assume that

all accreted convective rain feeds back to the resolvable scale. Once detrained, the accreted rain undergoes evaporation in a subsaturated environment. Since the accreted rain originates from deep convection, it descends to the ground in the downdraft core. We further assume that the accreted convective rain evaporates in a subsaturated environment by an amount that is proportional to the area of downdrafts. As will be shown in section 4, the accreted rain plays a dominant role in producing realistic precipitation amounts.

b. Initialization of the moisture field

Numerical simulations of MCSs on the meso-β scale have been shown to be critically dependent on two major factors: the inclusion of appropriate model physics and realistic initial conditions. Zhang and Fritsch (1986b) emphasized the importance of initial moisture and temperature fields in their simulation of a summertime mesoscale convective complex. Stensrud and Fritsch (1994), using a subjective mesoanalysis of moisture with the addition of mesoscale details, demonstrated a greater probability for a numerical simulation to succeed. The main deficiency of using the conventional analysis for meso-β-scale simulations of MCSs is the lack of mesoscale detail in both the temperature and moisture fields, due to the coarse horizontal resolution of the radiosonde network. This problem is particularly acute for the moisture field over the Tropics where observations are extremely sparse. One approach to the problem is the application of four-dimensional data assimilation. However, when the technique is applied to regions dominated by convection, such as in the western Pacific region, it is fraught with many difficulties (Stensrud and Bao 1992). Another approach, used successfully by Zhang and Fritsch (1986a) and Stensrud and Fritsch (1994), is to augment the observations using artificially constructed data.

We obtain our initial moisture condition using a two-step procedure. In the first step, we enhanced the moisture field of the operational ECMWF analysis by radiosonde observations using the PSU–NCAR MM5 preprocessor system. It is recognized that Lin and Johnson (1996) and Nuret and Chong (1996) have shown that relative to radiosonde measurements, the operational ECMWF analyses exhibit a systematic humidity excess in the lower troposphere and a systematic humidity deficit in the middle to upper troposphere over the TOGA COARE region. This moist bias in the 1000–900-hPa layer amounts to 0.5–1.0 g kg^{-1}. However, recent studies by Johnson and Ciesielski (2000) and Guichard et al. (2000) reported that a dry bias is present in the radiosonde system during TOGA COARE. From an analysis of data collected over three ship cruises aboard the *Moana Wave,* Guichard et al. (2000) concluded that the average measured specific humidity in the 1000–900-hPa layer is too dry by 0.75–1.5 g kg^{-1}. Therefore, at or close to radiosonde sites, our initial moisture con-

dition at low levels is too dry with respect to the true specific humidity over the TOGA COARE region. At a large distance away from radiosonde sites, the low-level specific humidity in our initial condition should not deviate by more than 0.5 g kg^{-1} from the true specific humidity.

In data-sparse regions, the ECMWF operational analysis is still likely to be too moist at low levels even when the dry biases in the radiosonde measurements are taken into account. This problem results from the use of diagnostic clouds in the radiation scheme in the ECMWF model, which tends to produce excessive low-level clouds (Slingo 1987). This problem becomes acute in data-sparse regions where the ECMWF analysis is biased toward the first guess fields. Tiedtke (1993) addressed this problem using a prognostic cloud scheme and showed a decrease of around 10% in relative humidity between 1000 and 500 hPa in the 10°N–10°S latitudinal band. In order to alleviate the problem we used the Barnes (1964) objective analysis scheme with a radius of influence of 125 km to set the relative humidity to 70% in the 1000–500-hPa layer over the data-sparse regions (indicated by D in Fig. 5). This procedure results in a reduction of relative humidity by 5%–10% between 1000 and 900 hPa, and by about 5% above 700 hPa. The maximum reduction is about 20% at 850 hPa.

The low moisture content at midlevels in the ECMWF analysis was corrected by inserting rainy period humidity profiles of Brown and Zhang (1997) between the 700- and 400-hPa levels (indicated by S in Fig. 5). The profiles were inserted in areas of deep convection as inferred by the presence of a brightness temperature ≤208 K at 2330 UTC 14 December 1992 (Fig. 5).

The warm-pool region exhibits significant diurnal variation in SST (Lukas 1991; Chen and Houze 1997; Fairall et al. 1996a). Cooper et al. (1996) observed that the 950-hPa mixing ratio changes by 1 g kg^{-1} for a step change in SST of 1°C (their Fig. 9). This provides a basis to improve the low-level (1000–900 hPa) moisture field at the model initial time, if the changes in SST can be estimated. In the present study, the SST changes at the model initial time (0000 UTC) are estimated by first obtaining the maximum amplitude in the diurnal SST change using the regression relation proposed by Webster et al. (1996). This amplitude depends on the daily averaged surface wind speed, precipitation rate, and the peak surface solar insolation. The daily averaged surface wind speed is determined from the 6-hourly ECMWF analysis for the 24-h period of 15 December 1992 starting at 0000 UTC. For simplicity, we set the daily precipitation rate to zero. This assumption is expected not to introduce significant errors in the SST amplitude estimates. For instance, the maximum daily precipitation rate during the entire IOP over the intensive flux array was 60 mm day^{-1} or 2.5 mm h^{-1} (Brown and Zhang 1997). This precipitation rate translates to an underestimation of only 0.07°C in the amplitude of SST. The peak surface solar insolation is computed, following

McNider et al. (1995), by utilizing the GMS satellite albedo measurements at 2230 UTC 14 December 1992. The maximum SST amplitude is about 2°C. Assuming a sinusoidal variation of SST with time and that the peak SST occurs at 1400 LST, an estimated warming of about 1.5°C occurs at the model initial time (0000 UTC or 1000 LST at 150°E).

In a second step, we used the regression relation suggested by Cooper et al. (1996) to relate the maximum SST amplitude to the amount of water vapor added in the 1000–900-hPa layer at the locations indicated by W in Fig. 5. This value turns out to be about 1.5 g kg^{-1}. Note that the W locations are close to a radiosonde site at Kapingamarangi. The moistening due to the SST correction would offset most of the dry bias in the radiosonde measurements in the 1000–900-hPa layer reported in Guichard et al. (2000).

4. Model verification

In this section, the results of the fine mesh run with the improved model physics and initial conditions are compared against all available observations, including point measurements from wind profilers, GMS satellite data, and airborne Doppler radar reflectivity and wind data collected during the mature stage of the MCS. More attention will be paid to the simulation of the general larger-scale environment, development of S_1 and S_2 and their merging into one MCS, as well as the generation of L_1 and L_2.

a. Validation against satellite measurements

The hourly GMS IR imagery could be used to verify the simulated cloudiness in terms of domain-averaged cloudiness and its time evolution during the growing stage (i.e., between 0600 and 1700 UTC). Recall that during this stage, the MCS initiates as two subsystems; each undergoes individual development and then merges to form an extensive anvil cloud cover that is seen to increase with time and attain its maximum by about 1830 UTC (see Fig. 1). Since the source of anvil cloud is deep convection, the cloud coverage gives a reasonable indication of the spread of convective activity over the region.

1) PERCENTAGE ANVIL CLOUD COVERAGE

Tollerud and Esbensen (1985) classified GATE cloud clusters into different stages on the basis of anvil cloud coverage. An anvil cloud was defined as present whenever the cloud fraction was greater than zero in a layer above 300 hPa. Here we choose the temperature at 300 hPa which is ≤ 243 K, as the threshold to define the presence of anvil clouds in the GMS satellite data (Fig. 14 in Kain and Fritsch 1990). For the model simulation, we assume that an anvil cloud occurs with the ice mixing ratio $q_i \geq 5 \times 10^{-3}$ g kg^{-1} in the 300–100-hPa layer.

The choice of the 300–100-hPa layer is consistent with that used by Tollerud and Esbensen (1985). For the threshold value, we noted that ice mixing ratio measured by McFarquhar and Heymsfield (1996, 1997) in tropical cirrus clouds varies with temperature and horizontal scale, ranging from 10^{-1} to 10^{-3} g kg^{-1} as the temperature changes from $-30°$ to $-70°$C. This suggests an average value for q_i in tropical cirrus clouds to be 5×10^{-2} g kg^{-1}. They also noted substantial horizontal variability in q_i on a horizontal scale of less than 100 km, with its peak near deep convective cores and a rapid decrease (nearly an order of magnitude) away from the convective cores. Since over a grid box of 20 km the area occupied by deep convection is relatively small, we estimate the threshold ice mixing ratio associated with cirrus clouds to be about 5×10^{-3} g kg^{-1}.

Figure 7 shows the percentage of anvil cloudiness over domain C (see Fig. 5) as a function of time. It takes about 2–3 h for the model to generate a reasonable amount of ice cloud content. Rapid rise in the cloud coverage occurs between 0900 and 1400 UTC when the MCS exhibits considerable areal expansion. The cloud coverage is maximized between 1700 and 2000 UTC (i.e., at the mature stage). Since the modeled anvil clouds are generated by ice detrainment from the KF CPS the general agreement with the GMS-derived anvil coverage indicates a realistic evolution of the simulated MCS. The anvil cloud fraction is in general larger than the observed and will be explained in section 5b. Its evolution will be further verified in more detail in the next section.

2) SPATIAL PATTERNS OF NEW CONVECTION

Sherwood and Wahrlich (1999) used time series of cloud fraction to determine convective onsets from the GMS IR satellite data [see section 3a(1)]. A model-simulated convective onset occurs when the total rain rate exceeds 3 mm h^{-1} for the first time within the previous 3 h over at least 5% of a 120-km box centered over a grid point. The choice of 3 mm h^{-1} as the threshold rain rate is motivated by the infrared brightness temperature versus rain rate relationship suggested by Sheu et al. (1996). In that study a mean rain rate of 3 mm h^{-1} is associated with a cloud-top temperature of 208 K. This rain rate is also consistent with that used by Nuret and Chong (1998) in their study of moisture budget of an MCS over the warm pool.

Figure 8 compares convective onset areas between the satellite-derived and the modeled precipitation. We point out that the first convective onset area for both the satellite and the model are obtained by requiring that the convective onset criteria be satisfied for the first time within the previous 2 h only because satellite data were not available before 0430 UTC and the model was initiated at 0400 UTC. These areas depict qualitatively the overall evolution of deep convection during the growing stage of the MCS. The simulated patterns of convective
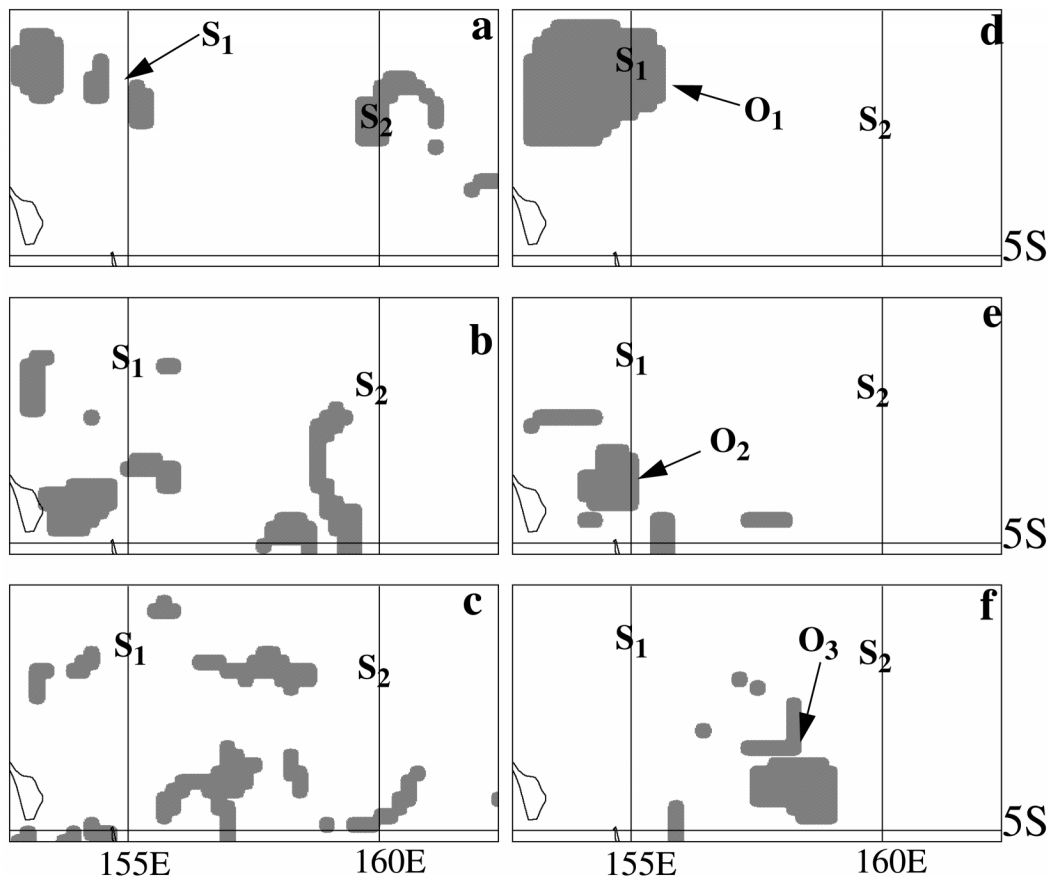
FIG. 8. New convective onset areas shown by shaded regions (a)–(c) for 0630, 1130, and 1430 UTC from GMS infrared imagery and (d)–(f) for 0600, 1100, and 1400 UTC from model simulation. The location of the entities S_1 and S_2 at 0530 UTC is indicated. Note that Kavieng Island enclosed by the solid contour lies at the lower-left corner of the figure panels.

onset at 0600 and 1100 UTC agree reasonably well with the observed (cf. Figs. 8a,d and 8b,e). However, the two simulated onset areas fail to capture the southern portion of the S_2 system partly due to the lack of observations in this area in the model initial conditions (cf. Figs. 8b,e). Nevertheless, the spatially more extensive system S_1 is in close agreement with observations at all the three times. The growing stage is marked by three convective onsets over three different regions, located over the respective areas of O_1 (0600 UTC), O_2 (1100 UTC), and O_3 (1400 UTC). These three convective onsets are responsible for the merger of the anvil that leads to a spatially extensive cold cloud shield during the mature stage. Convective onset in the model is governed by the convective trigger function criteria. The factors responsible for the three onsets will be discussed in a forthcoming article.

3) RADIATIVE CLOUD-TOP PRESSURE

The availability of GMS IR brightness temperature data allows the comparison of the observed radiative cloud-top pressure (CTP) with the model-simulated cloud-top pressure. The observed CTP is computed by determining the pressure at which the brightness temperature occurs using the simulated temperature profile. An IR sensor detects radiation from a cloud down to a depth corresponding to an emissivity approaching a value of unity. A mixed phase emissivity, e, is used following Garand and Nadon (1998). The simulated CTP is then defined to occur at a pressure at which $e = 0.99$.

The simulated CTP at 1800 UTC is compared against the observed at 1730 UTC (Fig. 9). The CTPs around 5°S, 160°E and around 5°S, 155°E are well simulated by the model. The model simulates smaller CTPs north of the equator due to deep convection occuring in these regions at 1800 UTC in contrast to larger CTPs associated with shallow clouds evident in Fig. 9b. Between 2.5°–5.0°S and 152.5°–160.0°E, observations reveal the presence of an area with CTP less than 200 hPa. The CTP increases on approaching the equator, except near 157.5°E, where smaller CTPs occur, followed by a decrease. Although the simulated CTP reveals more structure, a smaller region with CTP less than 200 hPa is
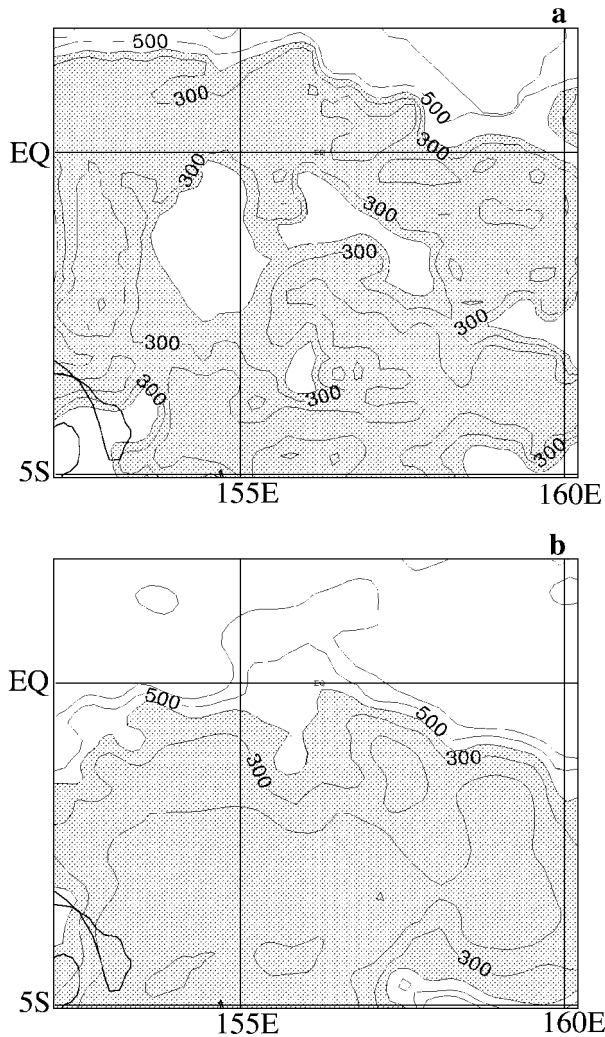
FIG. 9. The radiative cloud-top pressure in hPa from (a) model simulation at 1800 UTC and (b) GMS IR brightness temperature data at 1730 UTC. Cloud-top pressure lower than 400 hPa are shaded. Cloud-top pressure at 600–100 hPa are contoured every 100 hPa.

evident. There is fair agreement with the observed CTPs at other places, except for regions around 2.5°S, 160°E; 2.5°S, 157.5°E; 3°S, 156°E; and 0°–2.5°S, 155°E where the CTPs are larger (200–400 hPa; Fig. 9a). The simulated CTPs between 0°–2.5°S and 152.5°E are smaller than the observed. Since much of the cloud coverage in the simulation arises due to detrainment of cloud ice, cloud water, and rainwater from a convective cloud, larger CTPs in the simulation can result due to reduced strength of convection and/or a short-lived convective event and vice versa.

b. Validation against radar measurements

Airborne Doppler radar measurements by two National Oceanic and Atmospheric Administration P3 aircraft are used to verify the simulated MCS at the mature

stage. Protat et al. (1995, 1998) analyzed the Doppler radar winds and reflectivity fields over domain M shown in Fig. 5.

To facilitate the intercomparison of the simulated mesoscale structures with those reported by Protat et al. (1998), the high-resolution (5 km) radar data were coarsened to a horizontal resolution of 20 km. While horizontal resolution compatibility is achieved easily, it is difficult to mimic the sampling strategy used by the airborne Doppler measurements. The system L_1 was sampled by the aircraft between 1700 and 1830 UTC whereas the system L_2 was sampled between 1915 and 2045 UTC. The maximum range of the radar is 76.8 km, making it difficult to sample large areas of the MCS at the same time (A. Protat 1999, personal communication). Figure 10 compares the simulated reflectivity and wind field at 500 m at 1800 UTC; the former is converted from the simulated precipitation rate using the relation $Z = 323R^{1.43}$ (Short et al. 1997). Note that the rotation of the two domains differs by 15°. This added rotation accounts for the more east–west alignment of the simulated L_1 and L_2 against the NE–SW alignment observed by the radar.

During the mature stage, the numerical model produces convective elements inside the MCS. There are two convective lines with weak reflectivities lying to their northwest. The orientation of the convective lines, particularly the linear-shaped intense precipitation line L_1, is similar to that depicted in the radar observations. Because the two simulated lines are embedded in a large MCS and are the result of complex processes, a detailed analysis of the mechanism leading to their initiation and organization is required to demonstrate that they are the same two lines identified in the radar observations. We have completed such an analysis and our results showed that the MCS is initiated by a favorable SPTD and a vertical motion regulated by the confluence of the transequatorial flow and a quasi-2-day wave. We will report on these results in a future paper. The simulated magnitude for L_1 lies between 35 and 40 dBZ, while the observed values are 40–45 dBZ. Although system L_2 is simulated, the strong precipitation coverage is less conspicuous. The wind fields at 500-m height retrieved from the Doppler radar data and model simulation show large differences with the maximum magnitude differing by a factor of 2. The lack of parameterization of momentum transport can account partly for the weaker simulated wind speeds. Zhang and Cho (1991) proposed a cumulus parameterization procedure in which a horizontal pressure gradient force is induced by convective cloud buoyancy. The horizontal pressure gradient force points from the downdraft to the updraft in the low levels whereas it points in an opposite direction in the upper levels. This pressure gradient force can contribute to the acceleration of winds at low levels in the vicinity of deep convection, which represents an upgradient transport of horizontal momentum (Moncrieff 1992; Wu and Yanai 1994). Bearing in mind that the objective of
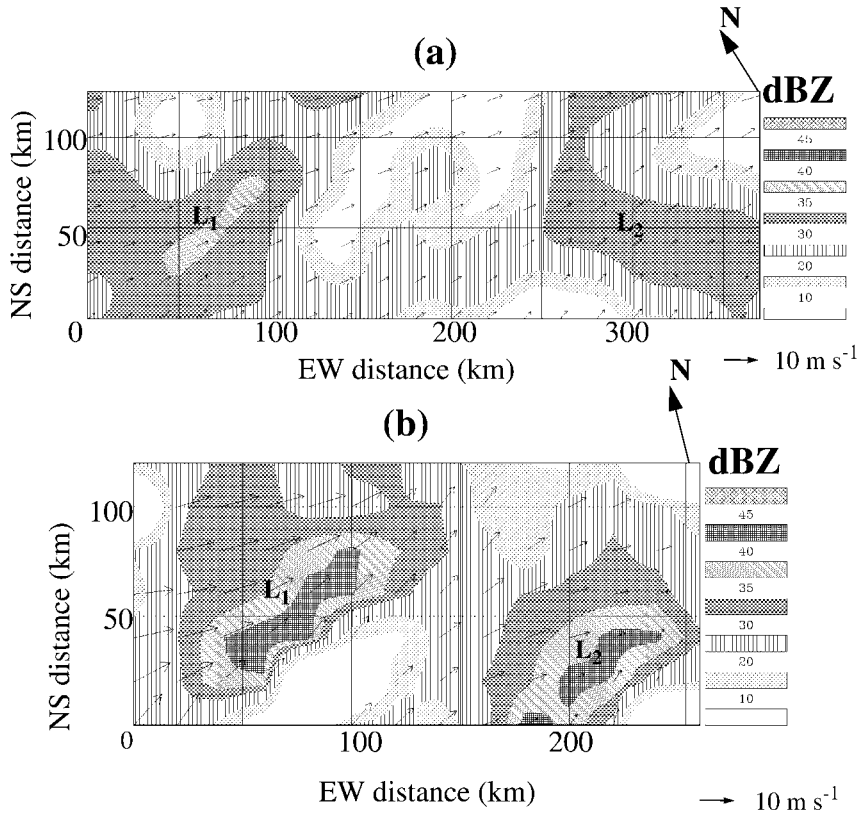
FIG. 10. (a) Model-simulated reflectivity at 1800 UTC along with horizontal winds at 500-m height. (b) Horizontal reflectivity and retrieved Doppler radar winds for the period between 1700 and 2045 UTC at 500-m height obtained from a mesoscale analysis of Protat et al. (1998). True north for both the domains are indicated as N. The lower-left corners of the domain in (a) and (b) are located at 4.45°S, 154.49°E and 4.28°S, 154.59°E, respectively.
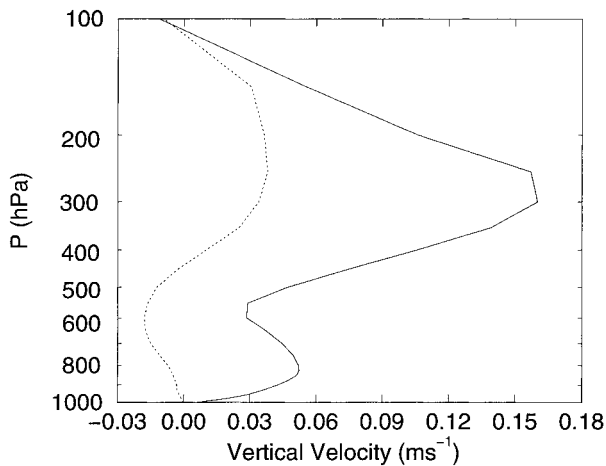

FIG. 11. Domain-averaged vertical velocity profiles in convective (solid) and stratiform (dashed) regions associated with the systems shown in Fig. 10. Convective region is defined by $Z > 35$ dBZ and stratiform region is defined by $Z < 30$ dBZ in Fig. 10.

this study is to simulate the mesoscale features associated with the MCS, the agreement between the simulated and observed radar reflectivity is deemed reasonable given the higher resolution of radar measurements and the coarse horizontal resolution of the simulation. We assume a simulated reflectivity greater than 35 dBZ (less than 30 dBZ) as representative of deep convection (stratiform precipitation). The deep convective regions exhibit two maxima (Fig. 11) consistent with the KF CPS heating profile for tropical soundings (Kain and Fritsch 1990). The stratiform precipitation regions exhibit mesoscale subsidence below the freezing level and ascent above. Protat et al. (1997) retrieved vertical profiles of horizontal divergence from the Doppler radar "purl" measurements. Each purl was approximately 5 km in radius and was mostly confined to stratiform regions of the systems. The vertical motion profile indicates subsidence below the 0°C level with mesoscale updrafts above. The peak mesoscale updrafts, located at about 8-km height, are 20–30 cm s^{-1}, while the peak downdrafts are -10 cm s^{-1}. The simulated values are one order of magnitude smaller, because of the averaging procedure and the coarse horizontal resolution of 20 km used in the simulation compared to the 5-km

mean radius for the purls used in the aircraft measurements.

c. Validation against wind profiler measurements

The integrated sounding systems (ISSs) were installed at several sites during TOGA COARE (Lin and Johnson 1996). Wind profiler measurements from the ISS sites are available at high temporal (every 30 min) and vertical (few hundred meters) resolution. For the purpose of our model validation, wind measurements from two ISS sites (i.e., Kapingamarangi and Kavieng; see Fig. 5 for their locations) located close to the MCS under investigation are chosen.

In general, the time evolution of the simulated horizontal wind patterns shows good agreement with the profiler wind. As previously mentioned, the MCS occurred about 2 weeks prior to the peak WWBs. Thus, the Kavieng station winds showed westerlies in the low level (Figs. 12a,b). The depth of westerlies and the backing of the low-level westerlies by roughly 180° between 0600 and 1000 UTC is well simulated by the model. Hourly streamline plots (not shown) between 0600 and 1000 UTC at 700 hPa reveal that this wind backing is caused by the westward migration of a transequatorial flow centered around Kavieng at 0400 UTC (Ramage 1971). On the other hand, Kapingamarangi lies just north of the equator and is in the easterly trade wind regime (Fig. 13). The MC2 model also reproduces the deep layer of easterly flow.

One may note that the simulated wind speeds are 1–2 m s^{-1} weaker than the observed. The discrepancies are more pronounced over Kavieng at most of the levels (Fig. 12). However, the 1–2 m s^{-1} discrepancies are within the measurement errors of wind profilers, as found by Riddle et al. (1996). Thus, we may state that the larger-scale flows in which the MCS is embedded are reasonably simulated.

5. Sensitivity study

Previous meso-β-scale modeling studies have demonstrated the importance of initial conditions and model physics. In this section, we examine the sensitivity of the model simulation to the convective trigger function and the modification of the moisture in the initial conditions.

a. Sensitivity to convective trigger function

Widespread convection occurs at many length scales over the western Pacific warm-pool region. Realistic prediction of deep convection for the tropical Pacific region remains a challenging task for meteorologists. The use of traditional stability indices, such as CAPE and the lifted index, often provides little indication about the occurrence of deep convection in these regions (Kodama and Businger 1998). In fact, the mesoscale-
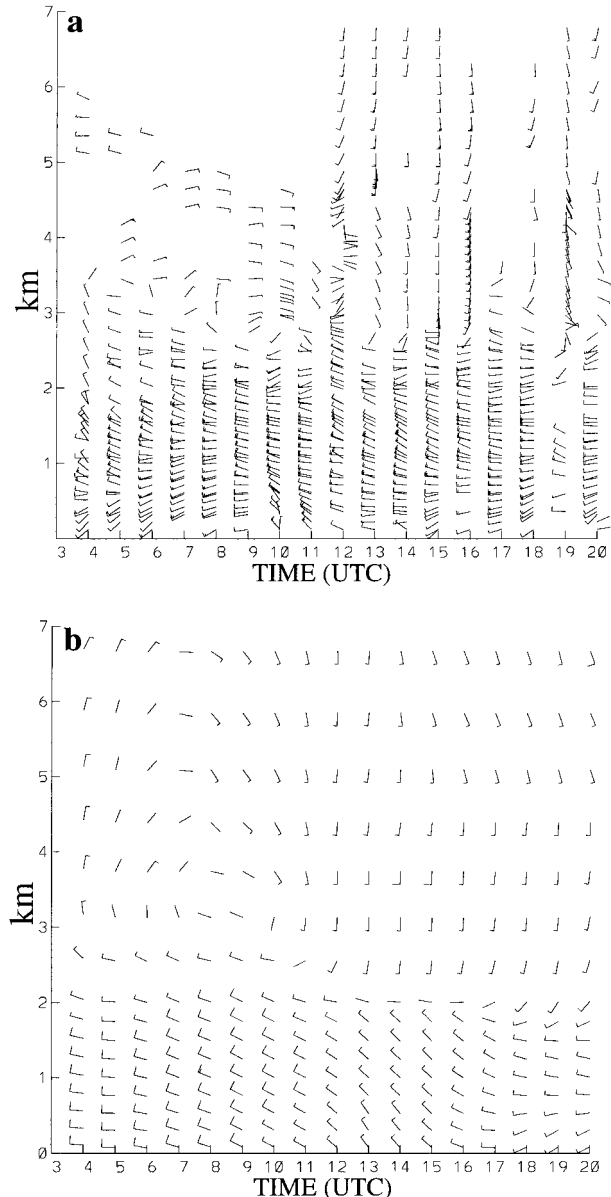

FIG. 12. Time–height cross sections of horizontal winds from (a) a wind profiler located at Kavieng (2.6°S, 150.8°E) and (b) a model grid point located at 2.8°S, 150.8°E. A full wind barb is 5 m s^{-1}.

mean CAPE sufficient for deep convection exists almost 90% of the time over the warm-pool region (Sherwood 1999).

Studies of Kain and Fritsch (1990) and Stensrud and Fritsch (1994) showed that numerical simulations of MCSs under weak-gradient environments are sensitive to convective initiation mechanisms used in mesoscale models. Refinements to the Fritsch and Chappell (1980) convective trigger function are reported in Rogers and Fritsch (1996). Addition of surface inhomogeneities to the trigger function offered a greater potential to successfully simulate MCSs in a variety of environments.
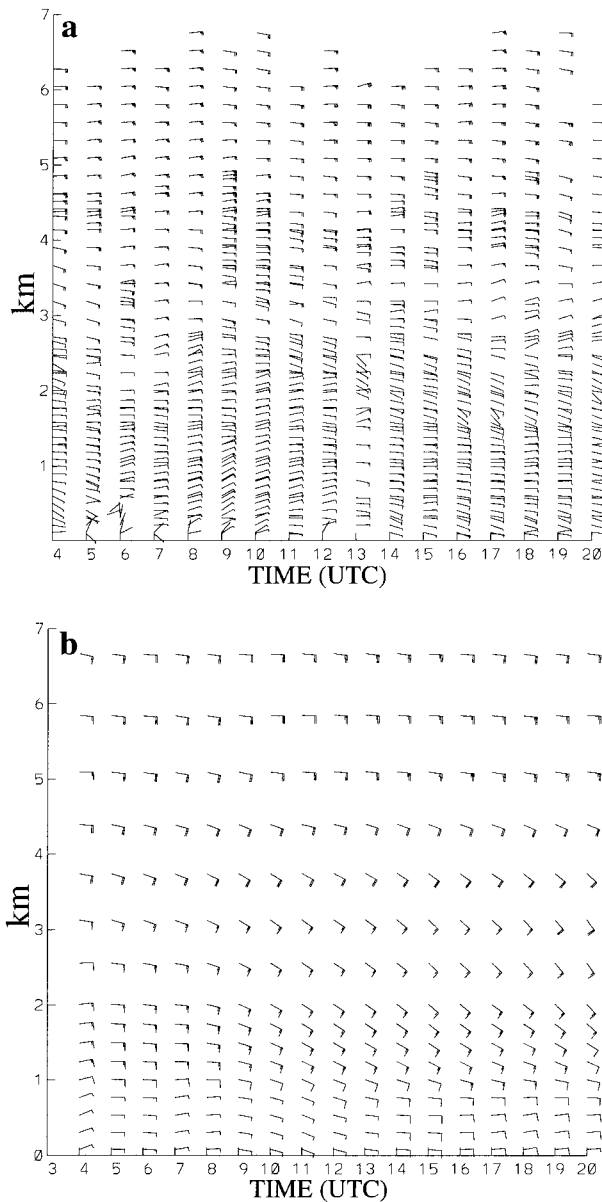
FIG. 13. As in Fig. 12 but for Kapingamarangi (1.1°N, 154.8°E). A full wind barb is 5 m s⁻¹.

TABLE 2. Sensitivity experiments performed with various combinations of the KFT function.

Expt	Remarks
KFT	Original KFT function
DCA	Original KFT function and deep column ascent
SPTD	Original KFT function and SPTD
CTL	Original KFT, deep column ascent, and SPTD

deep convective activity with a minimum during 1300–1400 UTC. It appears that the ABL recovers through the deposition of surface fluxes over the course of about 12 h, a result consistent with the Raymond (1995) quasi-equilibrium ABL hypothesis. After the recovery of the ABL, another round of deep convection occurs. The cloud fraction in the KFT experiment is larger than that in the DCA experiment, due to the added stringency in the DCA experiment by incorporating the criterion of DCA. The results of the KFT experiment suggest that long-term model integrations starting from the ECMWF analysis and the KF CPS tend to exhibit such sinusoidal temporal behaviors of deep convection over some regions.

The evolution of the cloud fraction in experiments SPTD and CTL shows similar behavior except that the peak cloud fraction in SPTD occurs around 1600 UTC compared to 1900 UTC in CTL. As expected, the cloud fraction is larger in SPTD due to the absence of the DCA criterion. As a result, the mature stage lasts from 1400 to 1900 UTC, in contrast to CTL, which lasts from 1700 to 2000 UTC. Thus, the original KFT function, complemented by the DCA and SPTD criteria, is responsible for the successful simulation of the life cycle of the MCS. The SPTD criterion has the biggest impact on the simulation of the life cycle, with the DCA acting to reduce the amount of convective activity during the

Thus, it is desirable to examine the sensitivity of the simulated MCS to the convective trigger function. For this purpose, three numerical experiments, as given in Table 2, using various combinations of the original KFT function and the two new criteria are performed.

Figure 14 shows the time evolution of cloud fraction over domain C. Experiments KFT and DCA exhibit a sinusoidal behavior of cloud fraction with time. Recall that the simulated anvil clouds are largely due to detrainment of ice particles from deep convection. This suggests a surge of widespread deep convective activity during the first few hours, resulting in the consumption of CAPE. The surge is followed by a period of little
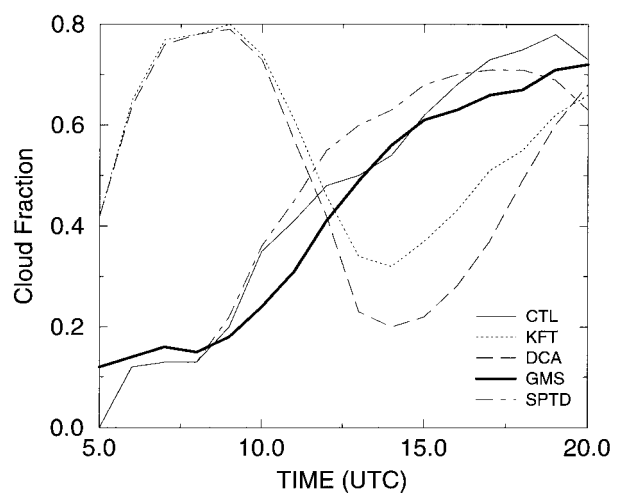

FIG. 14. Time evolution of the fractional cloud cover over domain C (see Fig. 5) for different sensitivity experiments associated with the convective trigger function. The thick solid line denotes the fractional cloud cover computed from GMS satellite data.
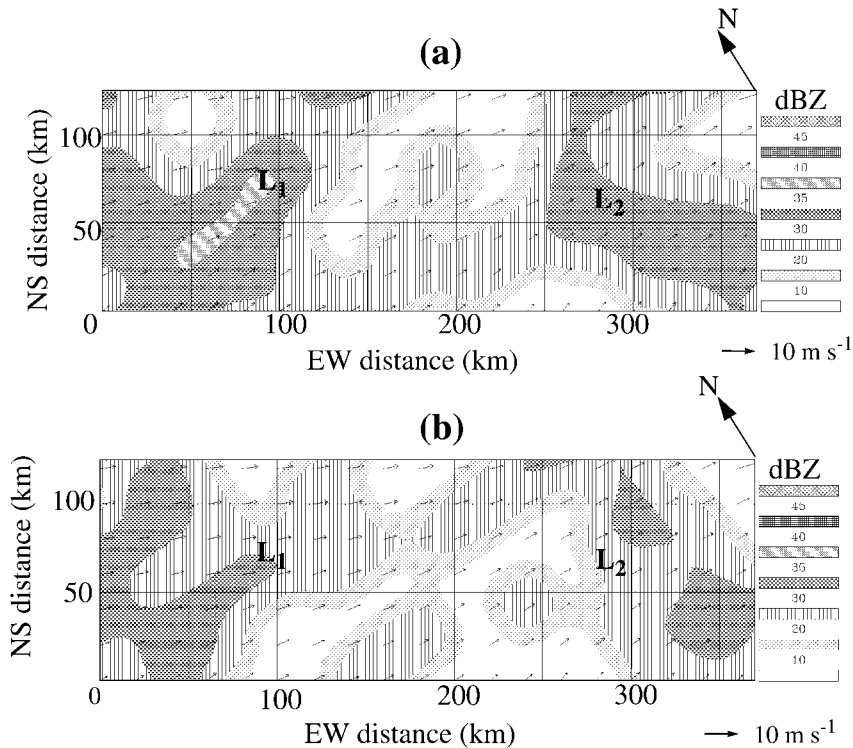
(a)

(b)

FIG. 15. Model-simulated reflectivity at 1800 UTC along with horizontal winds at 500-m height is shown for (a) the CTL simulation and (b) the SPTD trigger function sensitivity experiment. Model reflectivity is computed from total precipitation rate using the relation $Z = 323R^{1.43}$. True north for the domain is indicated as N. The lower-left corner of the domain is located at 4.45°S, 154.49°E.

growing stage, therefore yielding a better timing for the onset of the mature stage.

While the spatial distributions of convective onsets during the growing stage for CTL and SPTD are similar (not shown), there are differences in the structure of surface precipitation during the mature stage (1700–2000 UTC). The simulated radar reflectivity at 1800 UTC shows similar distribution between the two experiments but with weaker intensities occurring in the SPTD (Fig. 15). This may be due to the early onset of the mature stage resulting in the inclusion of some features associated with the dissipative stage of the MCS in SPTD.

TABLE 3. Sensitivity experiments performed with different initial moisture fields. The location of the D, S, and W data are shown in Fig. 5.

Expt	Remarks
CTL	Control simulation (with D, S, and W data)
ECM	Operational ECMWF analysis (without D, S, and W data)
NoD	Same as for CTL except with no D data
NoS	Same as for CTL except with no S data
NoW	Same as for CTL except with no W data

b. Sensitivity to initial moisture field

The sensitivity of the simulated MCS to the improvements in the initial moisture field is examined by performing four numerical experiments summarized in Table 3. The sensitivities of the simulation results are evaluated in terms of percentage anvil cloudiness over domain C and the spatial distribution of convective onsets.

Figures 16a and 16b show the evolution of the anvil cloud fraction and the fractional area occupied by deep convection, respectively. In the NoD and NoS experiments (Fig. 16a), the evolution of the cloud fraction between 0500 and 0800 UTC is similar to the CTL simulation, suggesting that in the presence of low-level moistening due to diurnal warming of SST (W data) the spinup period is significantly reduced. This is confirmed in the ECM and NoW experiments where lower cloud fractions occur between 0500 and 0800 UTC. The spinup period occurs between 0500 and 0600 UTC in experiments CTL, NoS, and NoD, while it extends from 0500 to 1000 UTC in the ECM and NoW experiments. The result suggests a decrease in the spinup period of about 3.5 h with the enhancement of low-level moisture due to diurnal warming of SST.

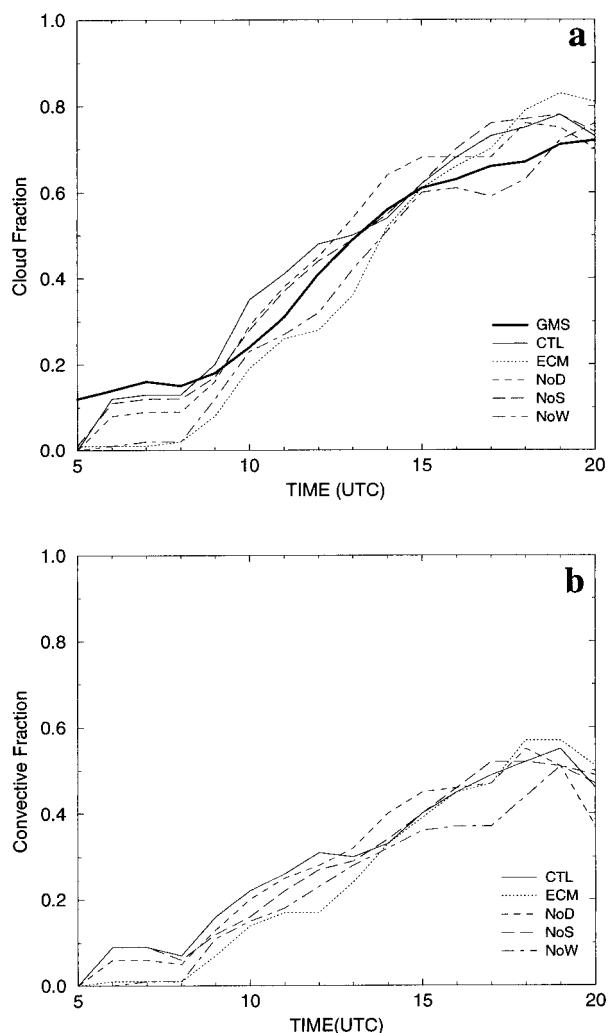The variation of the anvil cloud coverage among the

FIG. 16. (a) Evolution of the fractional anvil cloud cover over domain C (see Fig. 5) from hourly model output for the numerical experiments shown in Table 3. Shown in thick solid lines is fractional anvil cloud cover from hourly GMS infrared imagery. (b) The evolution of the fractional cover of deep convection over domain C for the numerical experiments.
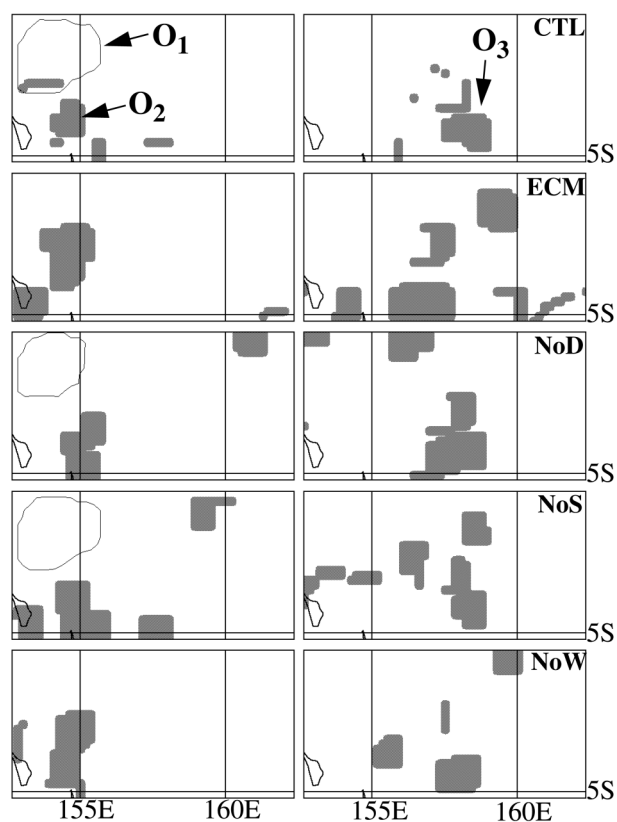

FIG. 17. All left-hand panels show the first and second convective onsets at 0600 and 1100 UTC, respectively, from the different sensitivity experiments summarized in Table 3. The first onset area is enclosed by a solid line and the second onset area is shaded. In the NoW and ECM experiments the first convective onset is absent. The convective onsets O_1, O_2, and O_3 in the CTL simulation are the same as in Fig. 8. The right-hand panels show the third convective onset (shaded) at 1400 UTC.

different sensitivity experiments arises largely due to the areal distribution of convective activity. Figure 16b shows that the fractional cover of convective activity over domain C exhibits similar evolution as the anvil cloud cover, suggesting that the anvil cloud cover arises mainly due to the detrainment of cloud ice, cloud water, and rainwater from convective clouds. In other words, the largest cloud fraction occurs in association with the most widespread convective activity and vice versa. This can account for the larger cloud fraction in the CTL simulation compared to observations (Fig. 7). In the CTL simulation, excessive low-level moistening by the W data can arise due to the overestimation of the peak surface solar insolation by neglecting the scattering and absorption effects of the atmosphere for solar radiation.

Figure 17 shows the first, second, and third convective onset areas from the different sensitivity experiments. The NoD run, which is similar to the CTL run, captures all three convective onsets. Spurious convective onsets are evident near 160°E at 1100 UTC and around 155°E at 1400 UTC, which are absent in the CTL simulation. The area of the third onset is larger than the CTL, leading to a larger anvil cloud fraction (Fig. 16a). Thus, the use of D data in improving the initial moisture field alleviates the problem of spurious convective activity and also yields more realistic anvil cloud coverage. In the NoS run, the three convective onsets are captured as in the CTL simulation though with a spurious onset occurring around 160°E at 1100 UTC. The use of S data in the initial moisture field impacts somewhat on the three convective onsets. This is as expected because the S data are far from S_1 and S_2 and confined to the 700–400-hPa layer.

In the NoW run, the first convective onset is not captured at 0600 UTC. As a result, the convective onset at 1100 UTC occupies some portion of the first onset. The

third convective onset is characterized by the appearance of two spurious onsets around 155° and 160°E, respectively. Therefore, in the absence of initial moistening at the lower levels at model initial time, the first convective onset is delayed by several hours, leading to an unrealistic evolution of deep convection.

In the ECM experiment, the first convective onset is also absent, leading to a second convective onset that is similar to the NoW experiment. Although the third convective onset qualitatively resembles the CTL experiment the structure of the surface precipitation at the mature stage (1700–2000 UTC) is very different from the CTL run. This result suggests the need to capture the first, second, and third convective onsets at the right place and time to obtain a realistic evolution of the system at the mature stage.

While CTL reproduces many of the observed features of the MCS during its mature stage, the location and orientation of systems L_1 and L_2 are fairly reproduced in the NoD and NoS experiments (not shown). In the NoW and ECM experiments the systems L_1 and L_2 are both poorly simulated in terms of the location, orientation, and strength (not shown).

6. Summary and conclusions

In this study, a 16-h meso-β-scale numerical study of the 15 December 1992 MCS was performed with a grid size of 20 km to demonstrate that with appropriate improvements to the initial moisture field and model physical representation, one can simulate realistically the life cycle of the MCS. The MCS under investigation occurred during the Australian monsoon season and 2 weeks prior to the peak westerly wind bursts. The satellite infrared imagery shows that the growing stage (0530–1700 UTC) was marked by the initiation of two entities (S_1 and S_2), which developed individually before merging into a spatially extensive MCS. The mature stage (1700–2000 UTC), observed by airborne Doppler radar, shows the presence of two lines (L_1, L_2) of deep convection with their associated stratiform regions to their rear. The stratiform regions exhibited descending motions below 3 km and ascending motion aloft. The decay of the MCS occurred around 2100 UTC when the area-averaged brightness temperature increases rapidly.

To attain a realistic simulation of the life cycle, we found it is necessary to improve the initial moisture field in the ECMWF analysis and some physical processes in the KF CPS. The initial moisture improvements address two deficiencies in the ECMWF data: excessive low-level moisture and very dry midlevels. In the vicinity of the MCS, the low-level moistening is introduced to reflect diurnal warming of SST. The improvements to the KF CPS include convective initiation, detrainment of cloud water and ice, convective rain formation by accretion and its detrainment, and other parameters used in the KF CPS. The KFT function is improved by the inclusion of two additional criteria: the DCA and the SPTD function. New

values are employed for the diurnal filter parameter (W_{klcl}), the constant C_1 used in computing the buoyancy of an air parcel at the lifting condensation level, and minimum cloud depth for deep convective initiation. The cloud water and ice contents in the deep convective cloud between cloud base and cloud top are accumulated and detrained in a 100–150-hPa layer at the cloud top. This results in a realistic evolution of the MCS anvil cloud coverage. Accretion of cloud water by convective rain is introduced as an additional rain production mechanism in the KF CPS. This rain is detrained to resolvable scales where it is assumed to undergo evaporation in a subsaturated environment depending on the area of the downdraft.

The simulated MCS was verified against satellite data during the growing stage. Good agreement was found in the evolution of the simulated anvil cloud fraction. Similar to the observations, the growing stage was composed of three convective onsets occurring at 0600, 1100, and 1400 UTC. The radiative cloud-top pressure associated with the MCS is in fair agreement with the satellite-observed cloud-top pressure. The model-simulated maximum reflectivity was between 35 and 40 dBZ against the observed maximum values of 40–45 dBZ. The two convective lines L_1 and L_2 observed during the mature stage are well simulated by the model. The orientation and strength of L_1 is reproduced by the model. Although L_2 is less well simulated in intensity and structure, the horizontal distribution of surface precipitation matches the observed. A comparison of the simulated 500-m wind speeds with those retrieved from the Doppler radar data reveals that the model winds are underestimated by about 50% likely due to the lack of momentum transport by cumulus convection in the KF CPS.

The model results are also compared to wind profiler measurements at Kavieng and Kapingamarangi. The simulated winds agree to within 1–2 m s^{-1} with the observed. The backing of the winds above 700 hPa between 0600 and 1000 UTC over Kavieng is also captured by the model and was associated with the westward migration of the transequatorial flow. A deep column of easterlies over Kapingamarangi is also well simulated by the model, suggesting that the large-scale flow in which the MCS is embedded is adequately captured.

The model-simulated life cycle is realistic with a reasonable reproduction of the growing and mature stages. Much of the success in the numerical simulation depends on incorporation of suitable trigger mechanisms for deep convection in the KF CPS. The sensitivity of the simulated results to the two additional criteria introduced into the KFT function was tested. A comparison of the simulation with the original KFT function and the SPTD criterion with the CTL simulation indicates that SPTD was largely responsible for the successful prediction of the life cycle of the MCS. However, inclusion of the DCA criterion yields a better timing for the onset of the mature stage (at 1700 UTC). Thus, a combination of the original KFT function with SPTD

MONTHLY WEATHER REVIEW

Volume 129

and the DCA criterion for convective initiation is necessary to successfully simulate the life cycles of the MCS. The SPTD criterion involves a specification of a threshold value for the occurrence of deep convection. The initial large-scale analysis of temperature, SST, and pressure along with the GMS IR satellite data over the previous 3 h are used to specify the threshold value. This suggests its possible use in operational numerical weather prediction (NWP) models to better forecast the timing and location of deep convection over the warm pool.

The sensitivity of the model-simulated life cycle is tested by systematically removing the moisture improvements introduced in the initial conditions. The low-level moistening due to the diurnal warming of SST at the model initial time helps to reduce the spinup time and capture the first convective onset. The reduction of relative humidity at the lower levels helps to alleviate the development of spurious convective activity in the simulation and hence yields a more realistic anvil cloud cover. The midlevel moistening impacts somewhat the three convective onsets as the modification is confined to midlevels and far from the location of the MCS. Using the ECMWF operational analysis alone, it was found that the anvil cloud cover, the timing and location of the three convective onsets, and the structure of precipitation during the mature stage are poorly simulated. The sensitivity experiments also suggest that the low-level moistening due to diurnal warming of SST may be a bit overestimated, causing the anvil cloud cover in the CTL simulation to be larger than the observed.

In conclusion, we may state that appropriate specification of the initial moisture field and use of suitable convective trigger mechanisms can improve significantly the accuracy in predicting convective developments and organization over the warm-pool region. While this study attempts to fill the gap that exists in the literature on the life cycles of the warm pool MCSs, clearly much remains to be done if all the remaining goals of COARE are to be attained. Godrey et al. (1998) in their COARE interim report suggested the need to produce high-resolution surface flux maps and wind fields to force ocean models that seek to replicate the response of the upper ocean. During COARE, observations from a variety of platforms were gathered and the assimilation of these observations using fine-resolution NWP models remains. This study suggests that appropriate specification of the initial moisture field and suitable convective trigger mechanisms can help in the attainment of these goals. Given the diverse modes of convective organization observed over the warm pool, future studies should include other numerical case studies.

REFERENCES

Barnes, S. L., 1964: A technique for maximizing details in numerical weather map analysis. *J. Appl Meteor.,* **3,** 396–409.

Benoit, R., M. Desgagne, P. Pellerin, S. Pellerin, Y. Chartier, and S. Desjardins, 1997: The Canadian MC2: A semi-implicit semi-Lagrangian wide-band atmospheric model suited for fine-scale process studies and simulation. *Mon. Wea. Rev.,* **125,** 2382–2415.

Betts, A. K., and M. J. Miller, 1993: The Betts–Miller scheme. *The Representation of Cumulus Convection in Numerical Models of the Atmosphere, Meteor. Monogr.*, No. 46, Amer. Meteor. Soc., 107–121.

Brown, R. G., and C. Zhang, 1997: Variability of midtropospheric moisture and its effect on cloud-height distribution during TOGA COARE. *J. Atmos. Sci.,* **54,** 2760–2774.

Chen, S. S., and R. A. Houze, 1997: Diurnal variation and life-cycle of deep convective systems over the tropical Pacific warm pool. *Quart. J. Roy. Meteor. Soc.,* **123,** 357–388.

Cooper, D. I., W. E. Eichinger, S. Barr, W. Cottingame, M. V. Hynes, C. F. Keller, C. F. Lebeda, and D. A. Poling, 1996: High-resolution properties of the equatorial Pacific marine atmospheric boundary layer from lidar and radiosonde observations. *J. Atmos. Sci.,* **53,** 2054–2075.

Crook, N. A., 1996: Sensitivity of moist convection forced by boundary layer processes to low-level thermodynamic fields. *Mon. Wea. Rev.,* **124,** 1767–1785.

Fairall, C. W., E. F. Bradley, J. S. Godfrey, G. A. Wick, J. B. Edson, and G. S. Young, 1996a: Cool-skin and warm layer effects on sea surface temperature. *J. Geophys. Res.,* **101,** 1295–1308.

——, ——, D. P. Rogers, J. B. Edson, and G. S. Young, 1996b: Bulk parameterization of air–sea fluxes for Tropical Ocean–Global Atmosphere Coupled Ocean–Atmosphere Response Experiment. *J. Geophys. Res.,* **101,** 3747–3764.

Fritsch, J. M., and C. F. Chappell, 1980: Numerical prediction of convectively driven mesoscale pressure systems. Part I: Convective parameterization. *J. Atmos. Sci.,* **37,** 1722–1733.

Garand, L., and S. Nadon, 1998: High-resolution satellite analysis and model evaluation of clouds and radiation over the Mackenzie basin using AVHRR data. *J. Climate,* **11,** 1976–1996.

Godrey, J. S., R. A. Houze, R. H. Johnson, R. Lukas, J.-L. Redelsperger, A. Sumi, and R. Weller, 1998: Coupled Ocean–Atmosphere Response Experiment COARE: An interim report. *J. Geophys. Res.,* **103,** 14 395–14 450.

Guichard, F., D. Parsons, and E. Miller, 2000: Thermodynamic and radiative impact of the correction of sounding humidity bias in the Tropics. *J. Climate,* **13,** 3611–3624.

Hagan, D., D. Rogers, C. Friehe, R. Weller, and E. Walsh, 1997: Aircraft observations of sea surface temperature variability in the tropical Pacific. *J. Geophys. Res.,* **102,** 15 733–15 747.

Houze, R. A., and A. K. Betts, 1981: Convection in GATE. *Rev. Geophys.,* **19,** 541–576.

Jabouille, P., J. L. Redelsperger, and J. P. Lafore, 1996: Modification of surface fluxes by atmospheric convection in the TOGA COARE region. *Mon. Wea. Rev.,* **124,** 816–837.

Johnson, R. H., and P. E. Ciesielski, 2000: Rainfall and radiative heating rates from TOGA COARE atmospheric budgets. *J. Atmos. Sci.,* **57,** 1497–1514.

Kain, J. S., and J. M. Fritsch, 1990: A one-dimensional entraining/detraining plume model and its application in convective parameterization. *J. Atmos. Sci., 47,* 2784–2802.
——, and ——, 1992: The role of the convective 'trigger' function in numerical forecasts of mesoscale convective systems. *Meteor. Atmos. Phys., 49,* 93–106.
——, and M. E. Baldwin, 1999: Parameterized convection and the quantitative precipitation problem. Preprints, *23d Conf. on Hurricanes and Tropical Meteorology,* Dallas, TX, Amer. Meteor. Soc., 870–872.
Kingsmill, D. E., and R. A. Houze, 1999: Kinematic characteristics of air flowing into and out of precipitating convection over the west Pacific warm pool: An airborne Doppler radar survey. *Quart. J. Roy. Meteor. Soc., 125,* 1165–1207.
Kodama, K. R., and S. Businger, 1998: Weather and forecasting challenges in the Pacific Region of the National Weather Service. *Wea. Forecasting, 13,* 523–546.
Kong, F. Y., and M. K. Yau, 1997: An explicit approach to microphysics in MC2. *Atmos.–Ocean, 35,* 257–291.
Leary, C. A., and R. A. Houze, 1979: The structure and evolution of convection in a tropical cloud cluster. *J. Atmos. Sci., 36,* 437–457.
——, and ——, 1980: Contribution of mesoscale motions to the mass and heat fluxes of an intense tropical convective system. *J. Atmos. Sci., 37,* 784–796.
LeMone, M. A., E. J. Zipser, and S. B. Trier, 1998: The role of environmental shear and thermodynamic conditions in determining the structure and evolution of mesoscale convective systems during TOGA COARE. *J. Atmos. Sci., 55,* 3493–3518.
Lin, X., and R. H. Johnson, 1996: Kinematic and thermodynamic characteristics of the flow over the western Pacific warm pool during TOGA COARE. *J. Atmos. Sci., 53,* 695–715.
Lukas, R., 1991: The diurnal cycle of sea surface temperature in the western equatorial pacific. *TOGA Notes, 2,* 1–5.
Mapes, B. E., 1993: Gregarious tropical convection. *J. Atmos. Sci., 50,* 2026–2037.
——, and R. A. Houze, 1993a: An integrated view of the 1987 Australian monsoon and its mesoscale convective systems. II: Vertical structure. *Quart. J. Roy. Meteor. Soc., 119,* 733–754.
——, and ——, 1993b: Cloud clusters and superclusters over the oceanic warm pool. *Mon. Wea. Rev., 121,* 1398–1415.
McBride, J. L., N. E. Davidson, K. Puri, and G. C. Tyrell, 1995: The flow during TOGA COARE as diagnosed by the BMRC tropical analysis and prediction system. *Mon. Wea. Rev., 123,* 717–736.
McFarquhar, G. M., and A. J. Heymsfield, 1996: Microphysical characterisitcs of three cirrus anvils sampled during the Central Equatorial Pacific Experiment. *J. Atmos. Sci., 53,* 2401–2423.
——, and ——, 1997: Parameterization of tropical cirrus ice crystal size distributions and implications for radiative transfer: Results from CEPEX. *J. Atmos. Sci., 54,* 2187–2200.
McNider, R. T., J. A. Song, and S. Q. Kidder, 1995: Assimilation of GOES-derived solar insolation into a mesoscale model for studies of cloud shading effects. *Int. J. Remote Sens., 16,* 2207–2231.
Miller, M., and J. M. Fritsch, 1991: Mesoscale convective complexes in the western Pacific region. *Mon. Wea. Rev., 119,* 2978–2992.
Molinari, J., and M. Dudek, 1992: Parameterization of convective precipitation in mesoscale numerical models: A critical review. *Mon. Wea. Rev., 120,* 326–344.
Moncrieff, M. W., 1992: Organized convective systems: Archetypal dynamical models, mass and momentum flux theory, and parameterization. *Quart. J. Roy. Meteor. Soc., 118,* 819–850.
Nakazawa, T., 1988: Tropical cloud clusters within intraseasonal variations over the western Pacific. *J. Meteor. Soc. Japan, 66,* 823–839.
Nitta, T., 1977: Response of cumulus updraft and downdraft to GATE A/B-scale motion systems. *J. Atmos. Sci., 34,* 1163–1186.
Numaguti, A., 1995: Characteristics of 4-to-20 day period disturbances observed in the equatorial Pacific during the TOGA COARE IOP. *J. Meteor. Soc. Japan, 73,* 353–377.

Nuret, M., and M. Chong, 1996: Monitoring the performance of the ECMWF operational analysis using the enhanced TOGA COARE observational network. *Wea. Forecasting, 11,* 53–65.
——, and ——, 1998: Characteristics of heat and moisture budgets of a mesoscale convective system observed during TOGA-COARE. *Quart. J. Roy. Meteor. Soc., 124,* 1163–1181.
Protat, A., Y. Lemaitre, and G. Scialom, 1995: Scale interactions involved in the initiation and evolution of mesoscale convective systems observed during TOGA COARE. Preprints, *27th Conf. on Radar Meteorology,* Vail, CO, Amer. Meteor. Soc., 734–736.
——, ——, and ——, 1997: Retrieval of kinematic fields using a single-beam airborne Doppler radar performing circular trajectories. *J. Appl. Meteor., 14,* 769–791.
——, ——, and ——, 1998: Thermodynamic analytic fields from Doppler-radar data by means of the MANDOP analysis. *Quart. J. Roy. Meteor. Soc., 124,* 1633–1668.
Ramage, C. S., 1971: *Monsoon Meterology.* Vol. 15. Academic Press, 296 pp.
Raymond, D. J., 1995: Regulation of moist convection over the west Pacific warm pool. *J. Atmos. Sci., 52,* 3945–3959.
Rickenbach, T. M., and S. A. Rutledge, 1998: Convection in TOGA COARE: Horizontal scale, morphology, and rainfall production. *J. Atmos. Sci., 55,* 2715–2729.
Riddle, A. C., W. M. Angevine, W. L. Ecklund, E. R. Miller, D. B. Parsons, D. A. Carter, and K. S. Gage, 1996: In situ and remotely sensed horizontal winds and temperature intercomparisons obtained using integrated sounding systems during TOGA COARE. *Contrib. Atmos. Phys., 69,* 49–61.
Rogers, R. F., and J. M. Fritsch, 1996: A general framework for convective trigger function. *Mon. Wea. Rev., 124,* 2438–2452.
Sherwood, S. C., 1999: Convective precursors and predictability in the tropical western Pacific. *Mon. Wea. Rev., 127,* 2977–2991.
——, and R. Wahrlich, 1999: Observed evolution of tropical deep convective events and their environment. *Mon. Wea. Rev., 127,* 1777–1795.
Sheu, R.-S., J. A. Curry, and G. Liu, 1996: Satellite retrieval of tropical precipitation using combined International Satellite Cloud Climatology project DX and SSM/I data. *J. Geophys. Res., 101,* 21 291–21 301.
Short, D. A., P. A. Kucera, B. S. Ferrier, J. C. Gerlach, S. A. Rutledge, and O. W. Thiele, 1997: Shipboard radar rainfall patterns within the TOGA COARE IFA. *Bull. Amer. Meteor. Soc., 78,* 2817–2836.
Slingo, J. M., 1987: Development and verification of a cloud prediction scheme for the ECMWF model. *Quart. J. Roy. Meteor. Soc., 113,* 899–927.
Stensrud, D. J., and J.-W. Bao, 1992: Behaviors of variational and nudging assimilation techniques with a chaotic low-order model. *Mon. Wea. Rev., 120,* 3016–3028.
——, and J. M. Fritsch, 1994: Mesoscale convective systems in weakly forced large-scale environments. Part II: Generation of a mesoscale initial condition. *Mon. Wea. Rev., 122,* 2068–2083.
Sui, C.-H., X. Li, K.-M. Lau, and D. Adamec, 1997: Multiscale air–sea interactions during TOGA COARE. *Mon. Wea. Rev., 125,* 448–462.
Tiedtke, M., 1993: Representation of clouds in large-scale models. *Mon. Wea. Rev., 121,* 3040–3061.
Tollerud, E. I., and S. K. Esbensen, 1985: A composite life cycle of nonsquall mesoscale convective systems over the tropical ocean. Part I: Kinematic fields. *J. Atmos. Sci., 42,* 823–837.
Webster, P. J., and R. Lukas, 1992: TOGA COARE: The Coupled Ocean–Atmosphere Response Experiment. *Bull. Amer. Meteor. Soc., 73,* 1377–1416.
——, C. A. Clayson, and J. A. Currie, 1996: Clouds, radiation, and the diurnal cycle of sea surface temperature in the tropical western Pacific. *J. Climate, 9,* 1712–1730.
Wu, X., and M. Yanai, 1994: Effects of vertical wind shear on the cumulus transport of momentum: Observations and parameterization. *J. Atmos. Sci., 51,* 1640–1660.
Zhang, D.-L., and J. M. Fritsch, 1986a: A case study of the sensitivity

of numerical simulation of mesoscale convective system to varying initial conditions. *Mon. Wea. Rev.,* **114,** 2418–2431.

——, and ——, 1986b: Numerical simulation of the meso-β-scale structure and evolution of the 1977 Johnstown flood. Part I: Model description and verification. *J. Atmos. Sci.,* **43,** 1913–1943.

——, E.-Y. Hsie, and M. W. Moncrieff, 1988: A comparison of explicit and implicit predictions of convective and stratiform precipitating weather systems with a meso-β-scale numerical model. *Quart. J. Roy. Meteor. Soc.,* **114,** 31–60.

Zhang, G. J., and H.-R. Cho, 1991: Parameterization of the vertical transport of momentum by cumulus clouds. Part I: Theory. *J. Atmos. Sci.,* **48,** 1483–1492.